IEEE Access
Multidisciplinary | Rapid Review | Open Access Journal

Received June 26, 2018, accepted July 31, 2018, date of publication August 10, 2018, date of current version September 7, 2018.

*Digital Object Identifier 10.1109/ACCESS.2018.2864800*

# First Dual MeV Energy X-ray CT for Container Inspection: Design, Algorithm, and Preliminary Experimental Results

**LIANG LI, (Senior Member, IEEE), TIAO ZHAO, AND ZHIQIANG CHEN**
Department of Engineering Physics and the Key Laboratory of Particle and Radiation Imaging, Ministry of Education, Tsinghua University, Beijing 100084, China
Corresponding author: Liang Li (lliang@tsinghua.edu.cn)

This work was supported in part by NSFC under Grant 11775124, Grant 61571256, Grant 11525521, and Grant 81427803, and in part by The National Key Research and Development Program of China under Grant 2017YFC0109103.

**ABSTRACT** Dual-energy mega-electron-volt (MeV) X-ray container radiography has become a well-established technique in customs security application, because of its material discrimination capability. The main difficulty of X-ray radiography is dealing with the materials overlapping problem. When two or more materials exist along the X-ray beam path, its material discrimination performance will be obviously affected. Computed tomography (CT) collects many X-ray measurements taken from different angles surrounding an object to produce cross-sectional (tomographic) images of the scanned object. Therefore, CT can provide real 3-D images inside the object. However, due to the bulky container volume and complex types of cargos, it is very hard to develop such a huge CT system for container inspection. To the best of our knowledge, there has no such commercial X-ray CT system for container inspection yet. This paper presents the design of a dual MeV energy X-ray CT system for cargo container inspection which uses an accelerator with fast 6/9 MeV switching spectra, an arc detector array and rotating mechanism. A dual MeV energy X-ray CT image reconstruction and material decomposition algorithm are developed. An experimental system was built with the same accelerator and detector array as used in the designed container CT system. Experimental results that prove the validity and effectiveness of the algorithm and CT system are presented.

**INDEX TERMS** Dual energy, X-ray radiography, container CT, image reconstruction, material decomposition.

## I. INTRODUCTION

Dual-Energy X-ray radiography has been widely used in security and customs applications, particularly for inspection of luggage, vehicles, and cargo containers in airports, stations, and harbors. It can obtain information on both the density and equivalent atomic number by using the specialized material discrimination algorithm from two radiographs acquired at two distinct X-ray spectra, helping us to determine the materials inside the object [1], [2]. Because the spectrum generated by the widely used X-ray tube or accelerator is polychromatic, dual-energy attenuation equations become nonlinear due to the beam-hardening phenomenon and are much more complex than the case of monochromatic X-ray imaging. In order to solve these nonlinear equations and identify the materials, Lehmann et al. proposed an analytic basis decomposition algorithm in the diagnostic energy range based on the two principle means of photoelectric absorption and Compton scattering [3]. In security application, curve-based material discrimination algorithms are often used in hundreds of kilo-electron volts (keV) or even several mega-electron volts (MeV) energy range, such as $R$-curve, H–L curve, and $\alpha$-curve algorithms [4]–[8]. They can stably calculate the equivalent atomic numbers of the penetrated materials using experimental dual-energy basis material calibration.

However, dual-energy radiography and its material discrimination methods can only provide correct results when there is only one unknown pure material along each X-ray path. When two or more overlapped materials, these mixed materials will be recognized as a new material with an equivalent atomic number $Z_{eq}$, which will occur false-positive or false-negative alarm in security inspection. For example, organic material held inside a thick iron box is easily misidentified as light metal. Chen *et al.* [9], [10] proposed a virtual peeling method to remove the background and reveal the material behind it. Li *et al.* [11] proposed a dynamic

material discrimination algorithm to solve this overlapping problem. However, the performances of these methods will be affected when the background has a strong texture or multiple materials exist along each X-ray path.

Computed tomography (CT) collects many X-ray radiographs taken from different angles surrounding an object to produce cross-sectional (tomographic) images of the scanned object [12]–[14]. It can provide real three-dimensional (3-D) images inside the object and completely solve the materials overlapping problem in cargo container radiography. Dual-energy CT (DECT), as well as multi-energy CT or spectral CT, takes advantages of CT and dual-energy configuration to provide more plentiful and accurate material information, e.g., electron density, equivalent atomic number and material composition. As the state-of-the-art CT imaging technique, dual keV energy X-ray CT has been successfully used in clinical diagnosis and airline baggage inspection. Usually, current keV DECT systems perform energy separations at X-ray source level such as dual-source technique, fast kVp switching and K-edge filtering, or separations at detector level such as the sandwich detectors and photon-counting detectors [15]–[20].

However, due to the bulky container volume and complex types of cargos, it is very hard to develop such a huge DECT system for container inspection. To the best of our knowledge, there has no such commercial CT product for container inspection yet. In this paper, we designs a dual MeV energy X-ray CT system for cargo container inspection which uses an accelerator with fast 6/9 MeV switching spectra, an arc detector array and rotating mechanism. We also develop a MeV DECT image reconstruction and material decomposition algorithm. Furthermore, we build an experimental system to evaluate our design and algorithm with the same accelerator and detector array as used in the designed container CT system. The organization of the remaining of this study is as follows: Section II presents physical model and reconstruction algorithm for MeV DECT imaging. Section III presents our design of 6/9 MeV DECT system. Section IV presents the real-data results on an experimental 6/9 MeV DECT system. Finally, Section V includes discussions and conclusions.

## II. METHODS

### A. PHYSICS MODELS OF MEV DECT

The physical principle of MeV DECT is based on the exponential law of photon radiation attenuation. When a polychromatic X-ray beam passes through an object, the detector signal can be described by the Beer–Lambert law. [21] If there are two different X-ray spectra used in DECT, we may get:

$$\begin{cases} I_L(ray_i) = \int_0^{E_L} S_L(E) \exp(-\int_{ray_i} \mu(\vec{x}, E) dl) dE \\ I_H(ray_i) = \int_0^{E_H} S_H(E) \exp(-\int_{ray_i} \mu(\vec{x}, E) dl) dE, \end{cases} \tag{1}$$

where $S_L(E)$ and $S_H(E)$ are effective spectra of low and high energy X-ray beams, respectively, which have considered the energy-dependent detector response and photon energy. $E_L, E_H$ are the maximum photon energy of these two spectra. $\mu(\vec{x}, E)$ is the linear attenuation coefficient of the scanned object locating in $\vec{x}$ and at an energy of $E$. $ray_i$ denotes the $i$-th X-ray path, and the inner integrals in Eq. (1) denote the line integrals along this $ray_i$.

Physically, the linear attenuation coefficient of a certain material can be decomposed linearly into four parts:

$$\mu(E) = [\sigma_{RS}(E) + \sigma_{PE}(E) + \sigma_{CS}(E) + \sigma_{PP}(E)] \cdot N_A \rho / A, \tag{2}$$

where $N_A$ is the Avogadro constant. $\rho$ denotes the mass density (g/cm$^3$). $A$ is the atomic weight of this material (g/mol). $\sigma_{RS}(E)$, $\sigma_{PE}(E)$, $\sigma_{CS}(E)$ and $\sigma_{PP}(E)$ are the energy-dependent cross sections of reactions from Rayleigh scattering, photoelectric effect, Compton scattering, and pair production, respectively.

Due to the huge volume of cargo container, MeV energy X-ray beam has to be used in its radiation imaging. In most of the current container inspection systems for radiography, the energy of the effective photons is usually 0.1–9 MeV, where Compton scattering predominates. In addition, as photon energy rises from 0.1 MeV to 9 MeV, the reaction cross sections of Rayleigh scattering and photoelectric effect decline significantly while pair production occurs and occupies an increasing proportion [11]. Therefore, different from keV DECT primarily considering photoelectric effect and Compton scatter, MeV DECT usually considers Compton scattering and pair production, and neglects photoelectric effect. Thus, $\mu(\vec{x}, E)$ of any material in Eq. (1) can be approximated as follows

$$\mu(\vec{x}, E) \approx a_{CS}(x) f_{CS}(E) + a_{PP}(x) f_{PP}(E), \tag{3}$$

where

$$\begin{cases} a_{CS} = \rho N_A Z / A \\ a_{PP} = \rho N_A Z^2 / A. \end{cases} \tag{4}$$

Where $a_{CS}$ and $a_{PP}$ are combination coefficients which are related to materials. $f_{CS}(E)$ and $f_{PP}(E)$ respectively denote the portions of the cross sections of Compton scattering and pair production which are related to photon energy. In the energy range of MEV DECT, $f_{CS}(E)$ and $f_{PP}(E)$ are proportional to $1/E$ and $E$, respectively, which can be theoretically calculated and experimentally measured [22]. In DECT, we usually define "electron density" $\rho_e = 2\rho Z / A$ (mol/cm$^3$). Thus, we get

$$\begin{cases} a_{CS} = \rho_e N_A / 2 \\ a_{PP} = \rho_e N_A Z / 2. \end{cases} \tag{5}$$

Actually, the accuracy of Eq. (3) depends largely on energy range of the incident X-ray beams. Because the energy range of effective photons in MeV DECT are very large, e.g., 0.1-9MeV, the accuracy of Eq. (3) is greatly affected.

Substituting Eq. (3) into Eq. (1) and taking the logarithm, we get the low and high energy projections

$$\begin{cases} p_L(ray_i) = \ln \int_0^{E_L} D_L(E) \exp\left[-A_{CS} f_{CS}(E) - A_{PP} f_{PP}(E)\right] dE \\ p_H(ray_i) = \ln \int_0^{E_H} D_H(E) \exp\left[-A_{CS} f_{CS}(E) - A_{PP} f_{PP}(E)\right] dE, \end{cases} \tag{6}$$

where $D_L(E)$, $D_H(E)$ are the normalized spectra. And,

$$\begin{cases} A_{CS} = \int_{ray_i} a_{CS}(\vec{x}) dl \\ A_{PP} = \int_{ray_i} a_{PP}(\vec{x}) dl. \end{cases} \tag{7}$$

Once $a_{CS}$, $a_{PP}$ are obtained by using the CT reconstruction algorithm from Eqs. (6) and (7), the materials parameters can be calculated at every position as follows

$$\begin{cases} \rho_e = 2a_{CS}/N_A \\ Z = a_{PP}/a_{CS}. \end{cases} \tag{8}$$

The above material decomposition model is based on the two photon cross sections of reactions from Compton scattering and pair production, which is also called dual-effect model. Dual-basis-material decomposition is another model frequently-used in DECT which assumes the linear attenuation function of any material can be accurately reproduced by a combination of two selected basis materials [23]. Thus, we have

$$\mu(E) = b_1 \mu_1(E) + b_2 \mu_2(E), \tag{9}$$

where $\mu_1(E), \mu_2(E)$ are the linear attenuation functions of two basis materials, and $b_1, b_2$ are decomposition coefficients.

The attenuation functions of each basis materials in Eq. (9) can be replaced by Eq. (3), we get

$$\mu(E) = (b_1 a_{CS1} + b_2 a_{CS1}) f_{CS}(E) + (b_1 a_{PP1} + b_2 a_{PP1}) f_{PP}(E) \tag{10}$$

Then, $\rho_e$ and $Z$ of the scanned object can be estimated by combining Eq. (3), Eq. (8) and Eq. (10):

$$\begin{cases} \rho_e = b_1 \rho_{e1} + b_2 \rho_{e2} \\ Z = \dfrac{b_1 \rho_{e1} Z_1 + b_2 \rho_{e2} Z_2}{b_1 \rho_{e1} + b_2 \rho_{e2}}, \end{cases} \tag{11}$$

where $\rho_{e1}$, $\rho_{e2}$ are the electron densities, and $Z_1, Z_2$ are the atomic numbers of the two basis materials numbered 1 and 2.

Again, substituting Eq. (9) into Eq. (1) and taking the logarithm, we get the low and high energy projections

$$\begin{cases} p_L(ray_i) = \ln \int_0^{E_L} D_L(E) \exp\left[-B_1 \mu_1(E) - B_2 \mu_2(E)\right] dE \\ p_H(ray_i) = \ln \int_0^{E_H} D_H(E) \exp\left[-B_1 \mu_1(E) - B_2 \mu_2(E)\right] dE, \end{cases} \tag{12}$$

where

$$\begin{cases} B_1 = \int_{ray_i} b_1(\vec{x}) dl \\ B_2 = \int_{ray_i} b_2(\vec{x}) dl. \end{cases} \tag{13}$$

Once $b_1, b_2$ are obtained by using the CT reconstruction algorithm from Eq. (12) and Eq. (13), the materials parameters can be calculated by Eq. (11) at every position.

### B. MEV DECT DECOMPOSITION AND RECONSTRUCTION METHOD

In DECT, there are mainly two kinds of decomposition and reconstruction methods: pre-processing method and post-processing method. The post-processing method first reconstructs the dual-energy CT images from different energy projections and then extracts the material fractions by decomposing the reconstructed attenuations into material components [24]–[28]. However, the performance of post-processing method often suffers from the artifacts within the CT reconstruction images, e.g., beam-hardening and metal artifacts [29], [30]. The pre-processing method first builds a dual-energy decomposition model like Eq. (3) or Eq. (9), and then converts the measured projections at different energies into the integrals of dual-effect model or dual-basis-material model like Eq. (6) or Eq. (12), respectively [31]–[34]. Each individual X-ray projection gives an independent equation set. Therefore, $A_{CS}, A_{PP}$ or $B_1, B_2$ along each X-ray path can be uniquely determined by solving Eq. (6) or Eq. (12). Then, the decomposition coefficients $a_{CS}, a_{PP}$ or $b_1, b_2$ can be reconstructed by using typical CT reconstruction algorithms, e.g., filtered-backprojection (FBP) or iterative reconstruction methods. Once $a_{CS}, a_{PP}$ or $b_1, b_2$ are obtained, the electron density and atomic number at every position can be calculated by using Eq. (8) and Eq. (11). The materials of the imaged object can be finally determined using these multiple information. This paper will focus on the pre-processing method as showed in Fig. 1.

The implementation of our MeV DECT reconstruction method is described as follows

Eq. (14) is a forward natural logarithm which can be easily implemented. $I_{L0}$, $I_{H0}$ are respectively the blank intensities of incident low-energy and high-energy X-rays without any object in the beams. Eqs. (15) and (16) are typical $l_2$ minimization problems which can be iteratively solved by using a classical optimization technique, such as

**Algorithm 1** Material Decomposition for Dual MeV Energy CT

**Input:** $I_L(ray_i)$, $I_H(ray_i)$, $I_{L0}$, $I_{H0}$, $S_L(E)$, $S_H(E)$

**Do:**

Pre-processing ray-by-ray in projection data domain

$$\text{Step1:} \quad \begin{cases} p_L(ray_i) = -\ln\left(I_L(ray_i)/I_{L0}\right) \\ p_H(ray_i) = -\ln\left(I_H(ray_i)/I_{H0}\right), \end{cases} \tag{14}$$

Step2: transfer the nonlinear equations to an optimization problem

$$(A_{CS}, A_{PP}) = \arg\min \left[p_L(A_{CS}, A_{PP}) - p_L\right]^2 + \left[p_H(A_{CS}, A_{PP}) - p_H\right]^2 \tag{15}$$

or

$$(B_1, B_2) = \arg\min \left[p_L(B_1, B_2) - p_L\right]^2 + \left[p_H(B_1, B_2) - p_H\right]^2 \tag{16}$$

CT reconstruction in image domain

Step3: reconstruct decomposition coefficients using FBP or iterative CT reconstruction algorithm

$$(A_{CS}, A_{PP}) \rightarrow (a_{CS}, a_{PP}) \tag{17}$$

or

$$(B_1, B_2) \rightarrow (b_1, b_2) \tag{18}$$

Step4: calculate the effective electron density and atomic number using Eq. (8) or Eq. (11)

**End**

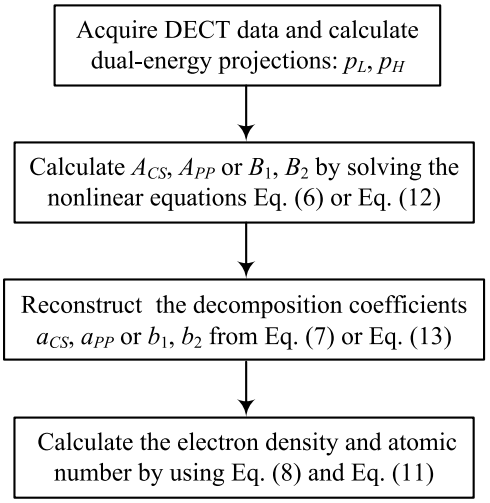


**FIGURE 1.** Flowchart of MeV DECT decomposition and reconstruction algorithm.

Gauss-Newton method. Eq. (17) and Eq. (18) are typical CT inverse problems which can be well reconstructed by using FBP, algebraic reconstruction technique (ART), or other model-based iterative algorithms [35]–[39]. Finally, the effective electron densities and atomic numbers of the imaged object can be calculated by Eq. (8) or Eq. (11) in every pixel/voxel.

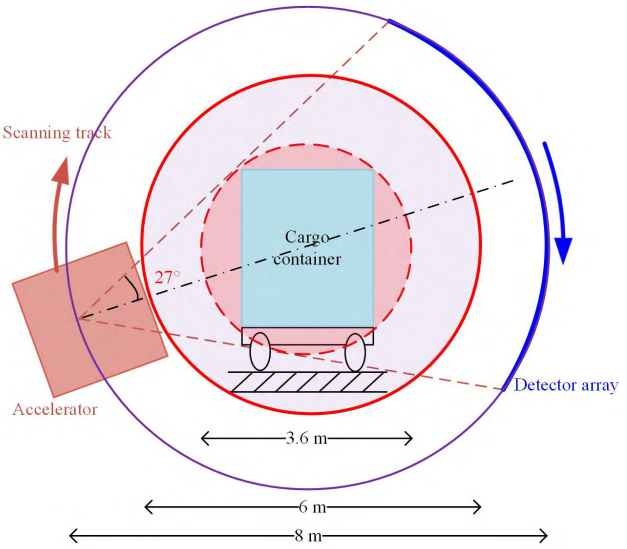


**FIGURE 2.** Schematic diagram of MeV DECT container inspection system.

## III. MEV DECT CONTAINER INSPECTION SYSTEM DESIGN

As mentioned in Section I, the overlap of different cargoes will obviously affect the performance of current dual-energy X-ray radiography product in container inspection. A better solution is a MeV energy CT system which exists in design but never comes true due to its high cost and huge size with very high technical difficulties [40], [41]. Our group try to develop the first MeV DECT container inspection system. As showed in Fig. 2, it uses a linear accelerator as the X-ray source which generates very fast switching electron pulses of 6 MeV and 9 MeV. An arc array detector is installed in the scanning track as well as the accelerator, all of which will be rotated vertically around a container truck. The data acquisition of this MeV DECT system follows the geometry of a conventional fan-beam CT scan. In order to avoid cable winding, a 234-degree half-scan is chosen which covers a field-of-view (FOV) of 3.6 m (diameter). This FOV ensures covering a 40-foot high cube container commonly used in sea-freight. The number of detector elements is 1504 with each detector pixel being 5 mm. The distance from the X-ray focal spot to the isocenter is 4 m and to the detector is 8 m. Projection data of 2340 views are collected and images are reconstructed with 2048×2048 pixels.

## IV. EXPERIMENTAL RESULTS

Before the designed MeV DECT container inspection system is manufactured, we built an experimental system with the same accelerator and detector array as used in the future container CT system. As showed in Fig. 3, the accelerator and detector array remained stationary, and the tested object was rotated on a turntable. The accelerator generated fast switching electron pulses of 6 MeV and 9 MeV with frequencies of 100 Hz + 100 Hz. The number of detector elements was 1280 with each detector pixel being 5 mm. The distance

**FIGURE 3.** A MeV DECT experimental system for Container Inspection.

from the X-ray focal spot to the isocenter was 4 m and to the detector was 6 m. Projection data of 1500 views were collected over 360 degrees and images were reconstructed with 1024×1024 pixels.

### A. SPECTRUM ESTIMATION OF X-RAY BEAM

As described in Eq. (6) and Eq. (12), the accuracy of the normalized X-ray beam spectra $D_L(E)$, $D_H(E)$ has a significant impact on DECT image reconstruction and material decomposition qualities. Usually, we use Monte Carlo simulation method to calculate an X-ray spectrum. However, in practice, errors always exist in this kind of simulated spectrum. The main reason is that it is very hard for a Monte Carlo simulator to model all physical parameters and uncertainties, e.g., all the noise sources and non-idealities in the detector and signal acquisition system. Therefore, $D_L(E)$, $D_H(E)$ has to be measured and calculated by specially designed experiments. In this paper, we designed a transmission measurement experiment for plates with seven different thicknesses and four different materials including carbon, aluminum, iron and lead which are frequently used and readily available. The mass thicknesses of these plates are 10, 30, 60, 90, 120, 150, 170 g/cm [2]. Therefore, we got 7×4=28 pairs low/high energy X-beam projections to estimate the effective spectra.

In the discrete case, the transmission projection data of low or high energy polychromatic X-ray can be described as

$$p_m = \frac{I_m}{I_0} = \sum_{n=1}^{N} D(E_n) \exp\left[-\mu(E_n) x_m\right] \tag{19}$$

where $m = 1, \cdots, M$ denoting the projection index of measurements. Here, $M = 28$. $x_m$ denotes the plate thickness used in the $m$-th measurement. $n = 1, \cdots, N$ denoting the index of spectrum samples. In this experiment, $N = 600$ for 6 MeV and $N = 900$ for 9 MeV, respectively. Eq. (19) can also be written in the matrix form

$$p_m = A_{mn} d_n \tag{20}$$

where $A_{mn} = \exp\left[-\mu(E_n) x_m\right]$ being a 2-D matrix. $d_n = D(E_n)$ denoting the normalized spectrum after discretization. As an underdetermined system of equations, Eq. (20) can be stably solved by using the expectation-maximization (EM) method [42].

Fig. 4 shows both initial and estimated normalized spectra of low and high energy beams. The red (low energy) and black (high energy) curves are normalized spectra simulated by Monte Carlo method, which are inputted as initial values into EM iteration algorithm. The blue and purple curves are estimated spectra of low and high energy, respectively. Due to the existences of detector energy response function, noise and other non-idealities, the effective spectra of both low and high X-ray beams are indeed very different from the initially incident X-ray spectrum obtained by Monte Carlo simulations. Therefore, considering the important role of spectrum in material decomposition, we believe spectrum calibration with experimental data is necessary.

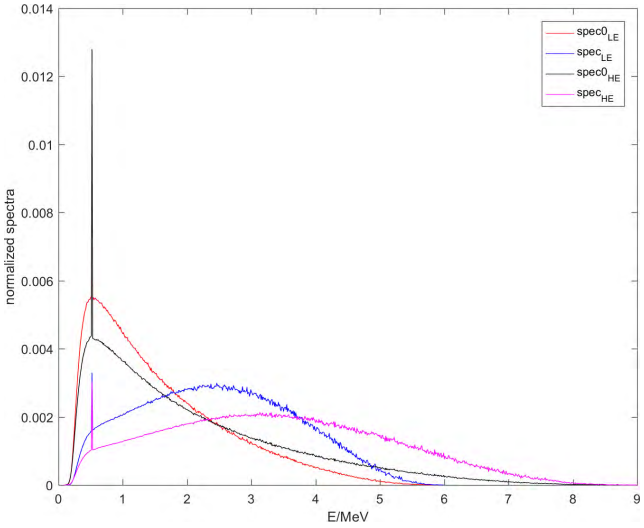


**FIGURE 4.** Normalized spectra used in the dual MeV container CT. "spec0$_{LE}$" and "spec0$_{HE}$" denote the simulated 6 and 9 MeV spectra by Monte Carlo method, respectively. "spec$_{LE}$" and "spec$_{HE}$" denote the estimated 6 and 9 MeV spectra by experimental measurements, respectively.

### B. MEV DECT IMAGE RECONSTRUCTION

In order to demonstrate the effectiveness of our experimental system and reconstruction method, we designed a test phantom as showed in Fig. 5. It included four columns. The orange and green columns were made of carbon and aluminum, respectively, with the same diameter of 200 mm. The blue and purple ones were made of iron and lead, respectively, with the same diameter of 100 mm. In the experiment, this phantom was placed and rotated in the center of FOV. Other scanning parameters were the same as that used in the designed MeV DECT container inspection system in Section III.

Dual-energy projection data and reconstructed images of the experiment were shown in Fig. 6. (a) and (b) were sinograms of low and high energy beams, respectively. (c) and (d) were corresponding CT reconstruction images whose values

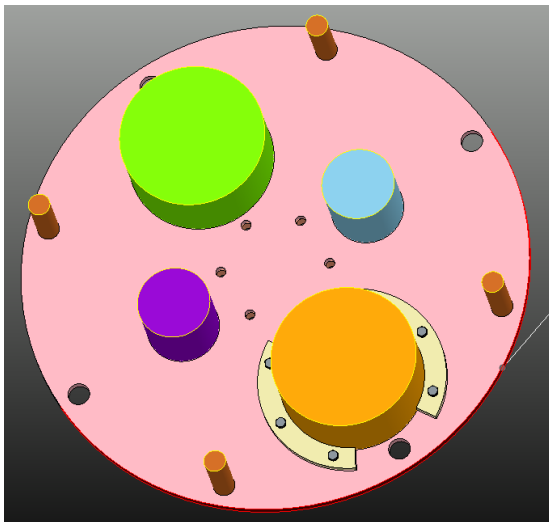

**FIGURE 5.** The test phantom used in our experiment which included four columns. The orange, green, blue and purple columns were made of carbon, aluminum, iron, and lead, respectively.

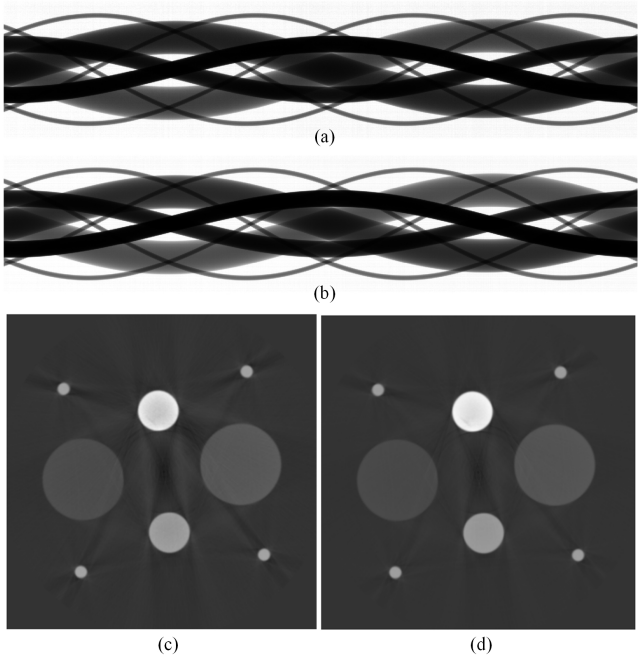


**FIGURE 6.** MeV DECT projection data and corresponding reconstruction images of the phantom in Fig. 5. The display window of (c) and (d) were [−0.01, 0.04].

represented the linear attenuation coefficients with a unit of $mm^{-1}$. The display window was set to $[-0.01, 0.04]$. We may find that the images were both well reconstructed from these two different sinograms. In low energy reconstruction there were some metal and beam-hardening artifacts while they were not obvious in high energy reconstruction.

We evaluated both of the two different MeV DECT decomposition and reconstruction methods as described in Section IIB. Results were shown in Figs. 7 and 8. Fig. 7(a) and (b) showed decomposed $A_{CS}, A_{PP}$ from

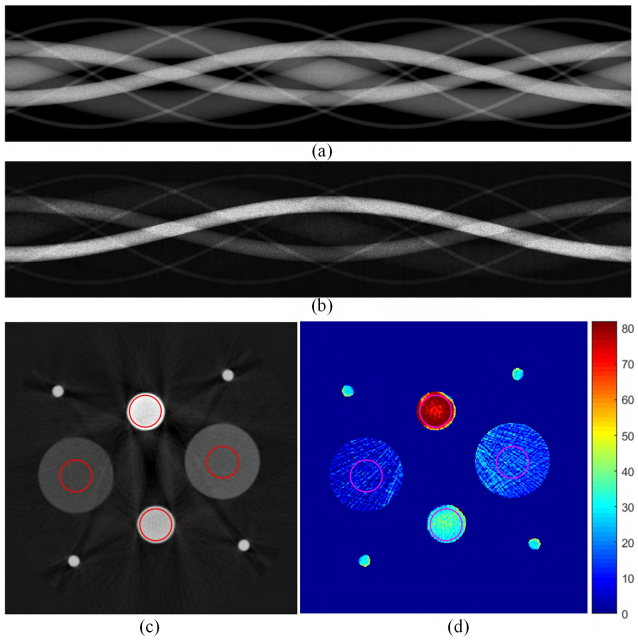


**FIGURE 7.** Decomposition and reconstruction results based on dual-effect model of Compton scattering and pair production. (a) and (b) were decomposed $A_{CS}, A_{PP}$ from DECT projections. (c) was the reconstruction of electron densities with a display window of [−1, 9]. (d) was the quantitative reconstruction of atomic numbers showed with a color map changing from blue to red along with increasing atomic numbers from 0 to 82.

DECT projections by solving the optimization problem of Eq. (15). DECT reconstruction results were showed in Fig. 7(c) and (d). (c) was the reconstruction of electron densities, i.e., $\rho_e$, with a unit of mol/cm [3]. The display window was set to $[-1, 9]$. It may be found that reconstruction of $\rho_e$ was very similar to low-energy or high-energy CT reconstructions showed in Fig. 6. Fig. 7(d) was the quantitative reconstruction of atomic numbers, i.e., $Z$, which was showed with a color map changing from cool tone to warm tone along with increasing atomic numbers from 0 to 82. Analogously, Fig. 8(a) and (b) were decomposed $B_1, B_2$ from DECT projections by solving the optimization problem of Eq. (16). (c) was the reconstruction of electron densities with the same display window as Fig. 7(c). (d) was the reconstruction of atomic numbers displayed with the same color map as Fig. 7(d).

Because the two material decomposition models, dual-effect model and dual-basis-material model, were very different, their corresponding decomposition results in projection domain differ widely too, as showed in Fig. 7(a, b) and Fig. 8(a, b). However, their DECT reconstruction results, Fig. 7(c, d) and Fig. 8(c, d), were similar. They both well reconstructed the electron densities, $\rho_e$, though there were some metal artifacts due to the existence of lead and iron columns in the phantom. The reconstruction quality of $Z$, was not as good as that of $\rho_e$. There were some streak artifacts in both Fig. 7(d) and Fig. 8(d). It can be seen that most of these streaks were divergent from the lead column.

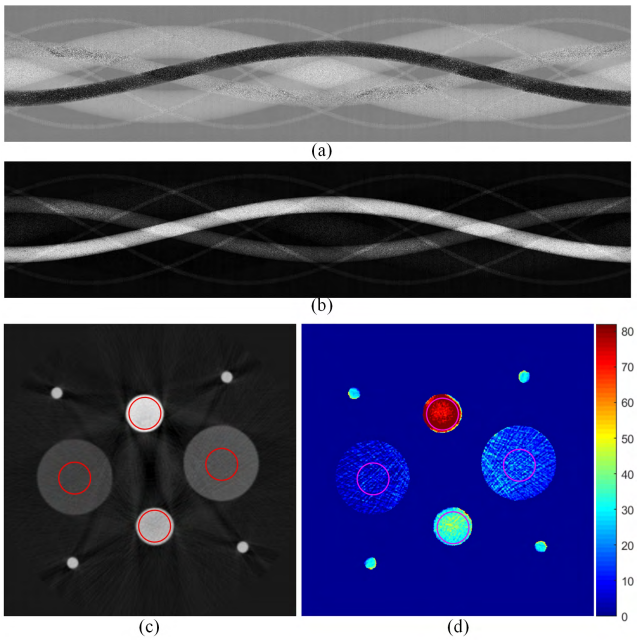


**FIGURE 8.** Decomposition and reconstruction results based on dual-basis-material model using carbon (Z=6) and tin (Z=50). (a) and (b) were $B_1, B_2$ decomposed from DECT projections. (c) was the reconstruction of electron densities with a display window of [−1, 9]. (d) was the quantitative reconstruction of atomic numbers showed with a color map changing from blue to red along with increasing atomic numbers from 0 to 82.

The reason was that the lead column with diameter of 100 mm strongly absorbed the incident X-ray beam, which caused only few photons reaching detector, i.e., photon starvation phenomenon [43]. Therefore, these artifacts in Fig. 7(d) and Fig. 8(d) are also called photon starvation streaks.

To quantify the dual MeV DECT reconstructions, we calculated the average mass densities and atomic numbers in the regions-of-interest (ROIs) marked by the red and purple circles as showed in Figs. 7 and 8. The mass densities, $\rho$ (g/cm$^3$), were shown in Table 1. Note that the electron density (mol/cm$^3$) has a different unit from mass density whose relationships were $Z = \rho_e A/2\rho$. The atomic numbers were shown in Table 2. We may find there were some obvious errors in both the results of mass densities and atomic numbers. The main reason was that the X-ray attenuation coefficients of different materials were very close in the photon energy range of several MeVs, which led to the ill-conditions of the dual-MeV decomposition equations, i.e., Eqs. (6) and (12). Furthermore, statistical noise and various artifacts, e.g., scattering artifacts, metal artifacts and beam hardening artifacts, increased the errors of dual-MeV CT reconstruction. In our experiments, the existence of the lead column brought serious photon starvation streaks which significantly affected the accuracy of both $\rho$ and $Z$ reconstructed results. In addition, the results of the Fe was worse than others. One possible reason was the iron metal used in the experiment contained certain impurities.

Comparing the quantitative results in Tables 1 and 2, it seemed that the results of dual-effect method were better than that of dual-basis-material method in the reconstruction accuracy, which still needed more experimental validations in the future.

**TABLE 1.** Mass density (g/cm$^3$) calculated from the dual MeV DECT reconstructions of Figs. 7(c) and 8(c).

| | C | Al | Fe | Pb |
|---|---|---|---|---|
| Truth (g/cm$^3$) | 1.80 | 2.70 | 7.80 | 11.40 |
| $\rho$ in Fig. 7(c) (g/cm$^3$) | 1.62 | 2.37 | 6.34 | 9.63 |
| $\rho$ in Fig. 8(c) (g/cm$^3$) | 1.62 | 2.34 | 6.02 | 9.21 |
| Errors of $\rho$ in Fig. 7(c) | 10% | 12.22% | 18.72% | 15.53% |
| Errors of $\rho$ in Fig. 8(c) | 10% | 13.33% | 22.82% | 19.21% |

**TABLE 2.** Atomic numbers calculated from the dual MeV DECT reconstructions of Figs. 7(d) and 8(d).

| | C | Al | Fe | Pb |
|---|---|---|---|---|
| Truth | 6 | 13 | 26 | 82 |
| $Z$ in Fig. 7(d) | 5.96 | 15.35 | 35.61 | 77.12 |
| $Z$ in Fig. 8(d) | 5.18 | 14.73 | 37.75 | 75.90 |
| Errors of $Z$ in Fig. 7(d) | 0.67% | 18.08% | 36.96% | 5.95% |
| Errors of $Z$ in Fig. 8(d) | 13.67% | 13.31% | 45.19% | 7.44% |

## V. DISCUSSION AND CONCLUSION

In this paper, we designed a dual MeV energy X-ray CT system for cargo container inspection. It used an accelerator with two fast switching spectra of 6 MeV and 9 MeV, an arc detector array and rotating mechanism. We built the physical models of this MeV DECT imaging system based on two different material decomposition approaches. Then, a MeV DECT decomposition and reconstruction method was developed. In order to evaluate the design and algorithm, we built an experimental system with the same accelerator and detector array as used in the designed container CT system. According to the experimental results, the validity and effectiveness of our MeV DECT CT system and algorithm were verified. Although the accuracies of $\rho$ and $Z$ decomposition results were influenced due to the existence of photon starvation in our experiment, we think our design and algorithm in this paper meet the preliminary demand of sea-freight container inspection. The designed MeV DECT container inspection system is being manufactured now. Further progress and results will be reported in the near future.

Note that whether dual-effect method or dual-basis-material method belongs to projection-domain decomposition method, which requires consistent dual-energy X-rays. However, in this paper the container CT system used a fast 6/9 MeV switching accelerator while the gantry continuously rotated. Hence, there was no such exactly consistent ray pairs, which led to the decomposition errors of both dual-effect and dual-basis-material models. We increased the sampling angle-views of CT scanning. Comparing with the effects of data noises and various artifacts on density/atomic number accuracies, the error due to the inconsistent X-rays can be neglected in this paper.

Aside from X-ray CT, there are several other 3-D imaging modalities which have been used or have potential

applications for container inspection, e.g., Muon tomography, Compton backscattering, nuclear resonance fluorescence technology (NRF), etc. These modalities have different merits and demerits. Limited by the cosmic Muon flux, Muon tomography needs longer data acquisition time, e.g., ten minutes or even more. Moreover, Muon tomography is only sensitive to heavy atoms like nuclear source materials. Compton backscattering imaging system usually has a more compact mechanical structure because its X-ray source and detectors are installed in one side and it detects the radiation reflecting from the target. Considering the radiation attenuation, the image quality of Compton backscattering deteriorates with the increasing detection depth. NRF system detects stimulated characteristic gamma rays emitted from nuclei, which belongs to quantified spectroscopy analysis technique. Usually, it is only used for heavy nuclei inspection such as uranium and thorium.

It is easy to accept that DECT is a much better solution than radiography to solve the very common problem of different cargoes overlap in container inspection. Although it needs high cost and solving a lot of technical difficulties, it can provide, indeed, a whole different perspective to visualize and quantitatively inspect container. Because scanning a whole container takes too much time, the container DECT designed in this paper only provides single-slice fan-beam CT scanning and imaging mode. In order to ensure a certain scanning rate, container DECT system will be applied as a secondary inspection tool if something suspicious is found in a container by dual-energy radiography.

## REFERENCES


[1] G. Chen, "Understanding X-ray cargo imaging," *Nucl. Instrum. Methods Phys. Res. B, Beam Interact. Mater. At.*, vol. 241, nos. 1–4, pp. 810–815, 2005.

[2] J. I. Katz, G. S. Blanpied, K. N. Borozdin, and C. Morris, "X-radiography of cargo containers," *Sci. Global Secur.*, vol. 15, no. 1, pp. 49–56, 2007, doi: 10.1080/08929880600993030.

[3] L. A. Lehmann *et al.*, "Generalized image combinations in dual KVP digital radiography," *Med. Phys.*, vol. 8, no. 5, pp. 659–667, 1981, doi: 10.1118/1.595025.

[4] S. Ogorodnikov and V. Petrunin, "Processing of interlaced images in 4–10 MeV dual energy customs system for material recognition," *Phys. Rev. Special Topics-Accel. Beams*, vol. 5, no. 10, p. 104701, 2002.

[5] G. W. Zhang, L. Zhang, and Z. Q. Chen, "An H-L curve method for material discrimination of dual energy X-ray inspection systems," in *Proc. IEEE Nucl. Sci. Symp. Conf. Rec.*, vol. 1, Oct. 2005, pp. 326–328.

[6] G. Chen, G. Bennett, and D. Perticone, "Dual-energy X-ray radiography for automatic high-Z material detection," *Nucl. Instrum. Methods Phys. Res. B, Beam Interact. Mater. At.*, vol. 261, nos. 1–2, pp. 356–359, 2007.

[7] V. L. Novikov, S. A. Ogorodnikov, and V. I. Petrunin, "Dual energy method of material recognition in high energy introscopy systems," in *Proc. 16th Int. Workshop Charged Part. Linear Accel.*, Alushta, Ukraine, 1999. [Online]. Available: https://www.kipt.kharkov.ua/conferences/ihepnp/16workshop/PDF/al9_705.pdf

[8] Y. Liu, B. D. Sowerby, and J. R. Tickner, "Comparison of neutron and high-energy X-ray dual-beam radiography for air cargo inspection," *Appl. Radiat. Isot.*, vol. 66, no. 4, pp. 463–473, 2008.

[9] G. Chen, J. Turner, D. Nisius, K. Holt, and A. Brooks, "Linatron Mi6, the X-ray source for cargo inspection," *Phys. Procedia*, vol. 66, pp. 68–74, Jan. 2015.

[10] G. Chen and D. Nisius, "High energy X-ray sources and detectors," in *Proc. 11th Workshop Adv. Develop. Secur. Appl. (ADSA)*. Boston, MA, USA: Northeastern Univ., Nov. 2014. [Online]. Available: https://myfiles.neu.edu/groups/ALERT/strategic_studies/ADSA11_Presentations/26_Chen.pdf

[11] L. Li, R. Li, S. Zhang, T. Zhao, Z. Chen, "A dynamic material discrimination algorithm for dual MV energy X-ray digital radiography," *Appl. Radiat. Isot.*, vol. 114, pp. 188–195, Aug. 2016.

[12] J. Hsieh, *Computed Tomography: Principles, Design, Artifacts, and Recent Advances*. Bellingham, WA, USA: SPIE Press, 2002.

[13] G. Wang, H. Yu, and B. De Man, "An outlook on X-ray CT research and development," *Med. Phys.*, vol. 35, no. 3, pp. 1051–1064, 2008.

[14] L. Li *et al.*, "An alternative derivation and description of Smith's data sufficiency condition for exact cone-beam reconstruction," *J. X-Ray Sci. Technol.*, vol. 16, no. 1, pp. 43–49, 2008.

[15] L. A. Lehmann and R. E. Alvarez, "Energy-selective radiography: A review," in *Digital Radiography*. New York, NY, USA: Springer, 1986, pp. 145–188.

[16] T. G. Flohr *et al.*, "First performance evaluation of a dual-source CT (DSCT) system," *Eur. Radiol.*, vol. 16, no. 2, pp. 256–268, 2006.

[17] D. Xu *et al.*, "Dual energy CT via fast kVp switching spectrum estimation," *Proc. SPIE*, vol. 7258, P. 72583T, May 2009, doi: 10.1117/12.811650.

[18] G. T. Barnes, R. A. Sones, M. M. Tesic, D. R. Morgan, and J. N. Sanders, "Detector for dual-energy digital radiography," *Radiology*, vol. 156, no. 2, pp. 537–540, 1985.

[19] R. E. Alvarez, J. A. Seibert, and S. K. Thompson, "Comparison of dual energy detector system performance," *Med. Phys.*, vol. 31, no. 3, pp. 556–565, 2004.

[20] L. Li, Z. Chen, W. Cong, and G. Wang, "Spectral CT modeling and reconstruction with hybrid detectors in dynamic-threshold-based counting and integrating modes," *IEEE Trans. Med. Imag.*, vol. 34, no. 3, pp. 716–728, Mar. 2015.

[21] J. Y. Chu, W. Cong, L. Li, and G. Wang, "Combination of current-integrating/photon-counting detector modules for spectral CT," *Phys. Med. Biol.*, vol. 58, no. 19, p. 7009, 2013.

[22] J. H. Hubbell, "Photon cross sections, attenuation coefficients, and energy absorption coefficients from 10keV to 100GeV," Nat. Bur. Standards, Washington, DC, USA, Tech. Rep. NSRDS-NBS 29, 1969.

[23] W. A. Kalender, W. H. Perman, J. R. Vetter, and E. Klotz, "Evaluation of a prototype dual-energy computed tomographic apparatus. I. Phantom studies," *Med. Phys.*, vol. 13, no. 3, pp. 334–339, 1986.

[24] F. Kelcz, P. M. Joseph, and S. K. Hilal, "Noise considerations in dual energy CT scanning," *Med. Phys.*, vol. 6, no. 5, pp. 418–425, 1979.

[25] H. J. Vinegar and S. L. Wellington, "Tomographic imaging of three-phase flow experiments," *Rev. Sci. Instrum.*, vol. 58, no. 1, pp. 96–107, 1987.

[26] B. J. Heismann, J. Leppert, and K. Stierstorfer, "Density and atomic number measurements with spectral X-ray attenuation method," *J. Appl. Phys.*, vol. 94, no. 3, p. 2073, 2003.

[27] K. Taguchi, M. Zhang, Eric C. Frey, J. Xu, W. P. Segars, and B. M. W. Tsui, "Image-domain material decomposition using photon-counting CT," *Proc. SPIE* vol. 6510, p. 651008, May 2007, doi: 10.1117/12.713508.

[28] L. Li *et al.*, "A tensor PRISM algorithm for multi-energy CT reconstruction and comparative studies," *J. X-Ray Sci. Technol.*, vol. 22, no. 2, pp. 147–163, 2014.

[29] M. M. Goodsitt, "Beam hardening errors in post-processing dual energy quantitative computed tomography," *Med. Phys.*, vol. 22, no. 7, pp. 1039–1047, 1981.

[30] D. J. Walter, E. J. Tkaczyk, and X. Wu, "Accuracy and precision of dual energy CT imaging for the quantification of tissue fat content," *Proc. SPIE*, vol. 6142, p. 61421G1, May 2006, doi: 10.1117/12.654669.

[31] R. E. Alvarez and A. Macovski, "Energy-selective reconstructions in X-ray computerised tomography," *Phys. Med. Biol.*, vol. 21, no. 5, pp. 733–744, 1976.

[32] S. J. Riederer and C. A. Mistretta, "Selective iodine imaging using k-edge energies in computerized x-ray tomography," *Med. Phys.*, vol. 4, no. 6, pp. 474–481, 1977.

[33] Y. X. Xing, L. Zhang, X. Duan, J. Cheng, and Z. Chen, "A reconstruction method for dual high-energy CT with MeV X-rays," *IEEE Trans. Nucl. Sci.*, vol. 58, no. 2, pp. 537–546, Apr. 2011.

[34] T. Zhao, L. Li, and Z. Chen, "K-edge eliminated material decomposition method for dual-energy X-ray CT," *Appl. Radiat. Isot.*, vol. 127, pp. 231–236, Sep. 2017.

[35] G. T. Herman, *Fundamentals of Computerized Tomography: Image Reconstruction from Projections*, 2nd ed. Dordrecht, The Netherlands: Springer, 2009.

[36] R. Gordon, R. Bender, and G. T. Herman, "Algebraic reconstruction techniques (ART) for three-dimensional electron microscopy and x-ray photography," *J. Theor. Biol.*, vol. 29, no. 3, pp. 471–481, 1970.

[37] M. Chang, L. Li, Z. Chen, Y. Xiao, L. Zhang, and G. Wang, "A few-view reweighted sparsity hunting (FRESH) method for CT image reconstruction," *J. X-Ray Sci. Technol.*, vol. 21, no. 2, pp. 161–176, 2013.
[38] L. Liu, "Model-based iterative reconstruction: A promising algorithm for today's computed tomography imaging," *J. Med. Imag. Radiat. Sci.*, vol. 45, no. 2, pp. 131–136, 2014.
[39] Z. Chen, X. Jin, L. Li, and G. Wang, "A limited-angle CT reconstruction method based on anisotropic TV minimization," *Phys. Med. Biol.*, vol. 58, no. 7, pp. 2119–2141, 2013.
[40] G. Zentai, "X-ray imaging for homeland security," in *Proc. IEEE Int. Workshop Imag. Syst. Techn.*, Chania, Greece, Sep. 2008, pp. 1–6.
[41] M. Salamon *et al.*, "Applications and Methods with High Energy CT Systems," in *Proc. 5th Int. Symp. NDT Aerosp.*, Singapore, Nov. 2013, pp. 1–8.
[42] E. Y. Sidky, L. Yu, X. Pan, Y. Zou, and M. Vannier, "A robust method of X-ray source spectrum estimation from transmission measurements: Demonstrated on computer simulated, scatter-free transmission data," *J. Appl. Phys.*, vol. 97, no. 12, p. 124701, 2005.
[43] I. Mori, Y. Machida, M. Osanai, and K. Iinuma, "Photon starvation artifacts of X-ray CT: their true cause and a solution," *Radiol. Phys. Technol.*, vol. 6, no. 1, pp. 130–141, 2013.

**LIANG LI** received the B.S. and Ph.D. degrees from Tsinghua University, Beijing, China, in 2002 and 2007, respectively. He is currently an Associate Professor with the Department of Engineering Physics, Tsinghua University. He has authored 130 peer-reviewed journals and conference papers. His research interests center on the mathematical and physical problems of X-ray imaging and its security, industrial, medical, and other applications, especially the reconstruction problems under the special imaging conditions.

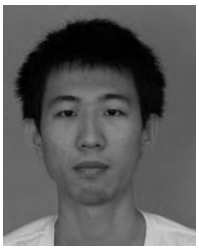

**TIAO ZHAO** was born in Taiyuan, Shanxi, China, in 1993. He received the B.S. degree from Tsinghua University, China, in 2016, where he is currently pursuing the Ph.D. degree. His current research interests include dual/spectral CT reconstruction and material decomposition.

**ZHIQIANG CHEN** received the Ph.D. degree in engineering physics from Tsinghua University Beijing, China, in 1999. He is currently a Professor with the Department of Engineering Physics, Tsinghua University. His research interests include x-ray imaging, computed tomography, image processing, and reconstruction.